Finite element simulation of high cycle fretting wear using an implicit adaptive cycle jump

Quentin Caradec, Matthieu Breuzé, Habibou Maitournam, Benoit Prabel, Jean-Luc Fayard

▶ **To cite this version:**

Quentin Caradec, Matthieu Breuzé, Habibou Maitournam, Benoit Prabel, Jean-Luc Fayard. Finite element simulation of high cycle fretting wear using an implicit adaptive cycle jump. Wear, 2023, 522, pp.204703. ⟨10.1016/j.wear.2023.204703⟩. ⟨cea-04218053⟩

HAL Id: cea-04218053

https://cea.hal.science/cea-04218053v1

Submitted on 20 Dec 2023

HAL is a multi-disciplinary open access archive for the deposit and dissemination of scientific research documents, whether they are published or not. The documents may come from teaching and research institutions in France or abroad, or from public or private research centers.

L'archive ouverte pluridisciplinaire **HAL**, est destinée au dépôt et à la diffusion de documents scientifiques de niveau recherche, publiés ou non, émanant des établissements d'enseignement et de recherche français ou étrangers, des laboratoires publics ou privés.

HAL Authorization

Finite element simulation of high cycle fretting wear using an implicit adaptive cycle jump

Quentin Caradec[a,b], Matthieu Breuzé[a,b], Habibou Maitournam[b], Benoit Prabel[a,b] and Jean-Luc Fayard[a,b]

[a] Université Paris-Saclay, CEA, Service d'Études Mécaniques et Thermiques, 91191, Gif-sur-Yvette, France
[b] IMSIA, ENSTA Paris, CNRS, EDF, CEA, Institut Polytechnique de Paris, 91762, Palaiseau Cedex, France

ARTICLE INFO

Keywords:
Fretting
Wear
Finite element
Implicit scheme
Cycle jump

ABSTRACT

Fretting motion between two contacting solids can, under gross slip conditions, induce wear. A finite element model and a simulation strategy aiming at predicting wear under fretting motion are presented. The numerical results obtained are compared with experimental data from the literature. The proposed simulation process is particularly suitable for computing high numbers of cycles. To this end, a cycle jump technique is used, and different integration schemes are investigated. Results show that instabilities may arise when an explicit scheme is used, which limits the size of the cycle jump. On the other hand, using an implicit scheme involves a trade-off between the possibility of considering a larger cycle jump and the number of iterations required for convergence. It is shown that the more cycles we perform, the faster the implicit scheme converges. Therefore, the implicit scheme is especially appropriate for high-cycle computations. Moreover, an adaptive cycle jump is used with the implicit scheme, enabling to accelerate the computations for high numbers of cycles.

1. Introduction

Wear is a progressive surface degradation process that results in material removal. It occurs in numerous engineering systems as a result of mechanical and chemical solicitations and can significantly reduce the lifetime of industrial components. Among the various mechanisms likely to generate wear, fretting refers to small amplitude cyclic tangential motions between two contacting solids. Different fretting regimes can be identified, each leading to different damage modes [1]. For the lowest displacement amplitudes, the partial slip regime defines a situation in which an inner stick zone in the contact area never slides. For higher displacement amplitudes, the gross slip regime is characterized by a contact area with no stick zone. Fretting maps relate fretting regimes to damage modes [2]. Partial slip generally leads to crack nucleation and propagation, whereas wear typically prevails under gross slip conditions.

Fretting is inherent to a variety of industrial mechanisms, including some components of nuclear reactors [3]. In pressurized water nuclear reactors (PWR), the guide cards of the rod cluster control assemblies are prone to wear as a consequence of repeated contacts with the control rods [4]. This case illustrates a situation of wear occurring under fretting motion between stainless steel (SS) components. In the scope of this study, the focus is on wear occurring under gross slip fretting conditions between stainless steel solids, meant to represent the contact between control rods and guide cards.

Due to the diversity of physical and chemical processes involved, wear is a complicated phenomenon to model [5]. One of the first attempt to propose a unified wear law was made by Archard in 1953, and relates the wear volume to the normal force and the sliding distance [6]. Later, studies by Fouvry et al. [7] then Huq and Celis [8] showed that an energetic wear model correlating wear to the energy dissipated by friction was more reliable, in particular when the friction coefficient is not constant. More recent works outline the effect of other mechanisms on fretting wear rate. According to Archard's model, wear rate is related to particles detachment from the surfaces and is assumed to be constant throughout the evolution of the surfaces shapes. Zhu et al. [9] point out that in case of non-conforming surfaces, the evolution of the wear scar size has an effect on wear rate due to the more difficult ejection of debris out of the contact. They derive a modified relation between wear volume and dissipated energy that is found to be more reliable when debris ejection happens to be the rate-determining process. In addition, Baydoun et al. [10] consider the effect of oxygen transport into the contact interface and develop an advection-dispersion-reaction model. Based on this approach, they differentiate locally adhesive wear from abrasive wear by considering the partial pressure of di-oxygen in the contact. These two recent advances were brought together in 2021 in an article by Shipway et al. [11]. Depending on the rate-determining process, they argue that wear rate decreases with increasing contact width.

Following the initial work by Johansson in 1994, different studies proposed numerical frameworks for predicting wear [12]. Most rely on the finite element method to compute the incremental evolution of wear, based either on Archard's law or on the energetic wear model, and represent wear by nodal displacements [13, 14, 15, 16, 17, 18]. They dealt with the need to compute very high numbers of time steps by using an acceleration factor [14]. In case of a cyclic loading, it is equivalent to the cycle jump technique which aims at computing wear on a limited number of cycles by extrapolating the results from a single cycle over the next cycles. It requires to introduce an acceleration factor that defines the jump between two consecutive computed cycles.

The acceleration factor can be supposed either constant or variable [15]. Moreover, although most numerical models are two-dimensional and suppose an elastic material behavior, three-dimensional models have also been proposed [16] as well as the consideration of an elastoplastic material behavior [19, 20]. Yang and Green [21] compute wear profiles based on Archard's law as a consequence of fretting loading considering an elastic-perfectly plastic material behavior, but their work only relies on the computation of a few cycles and do not account for the evolution of contact geometry. More recent studies include other features such as the representation of third body in the interface [20, 22] or a porous coating [23]. The advection-dispersion-reaction model proposed by Baydoun et al. [10] has also been implemented in a finite element analysis of fretting wear [24]. Some authors also used these numerical models to study the competition between wear and crack nucleation and propagation under fretting motion [25].

In this paper, a numerical framework based on the finite element method is proposed to compute high-cycles fretting wear. The results will be compared to experimental data obtained by Marc [26] on a AISI 316L SS/AISI 304L SS cylinder/plane contact. The main difficulty lies in the need to simulate a high number of cycles at a low contact pressure. To this end, a cycle jump technique is used. As related in previous studies [15, 17], this can lead to unexpected fluctuations in the computed surface pressure when the acceleration factor is high. In order to significantly accelerate the computation without deteriorating the surface smoothness, the use of a backward Euler implicit scheme is proposed in this work. The computation strategy is similar to existing methods used for fatigue simulations [27]. Besides the implicit scheme, an original method using an adaptive cycle jump is proposed.

The experimental setup and results are presented in Section 2, while Section 3 describes the finite element model. The wear simulation process is discussed in Section 4 with the presentation of the cycle jump method and the explicit and implicit integration schemes. Finally, the results obtained are compiled and discussed in Section 5.

2. Experimental data and wear model

2.1. Experimental data

Experimental data summarized hereafter were obtained by Marc et al. [28, 29, 26]. Fretting wear tests were carried out on an unlubricated cylinder/plane contact at room temperature (Figure 1). The cylinder is made of nitrided AISI 316L stainless steel, while the plane is made of AISI 304L stainless steel. The cylinder has a length $L_0 = 10$ mm and a radius $R = 4.85$ mm. A constant normal load and an oscillating tangential displacement at frequency $f = 5$ Hz are imposed. Several tests are run, varying the normal load P between 2 N/mm and 5 N/mm, the displacement amplitude δ between 40 µm and 160 µm, and the number of fretting cycles between 25,000 and 1,500,000.

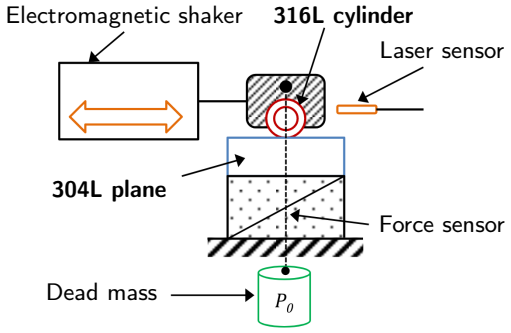

Figure 1: Experimental setup for the fretting wear tests [26].

The tangential force F_T and the horizontal displacement δ are recorded through the tests. The fretting log representing the evolution of the tangential force with respect to the displacement over the cycles is depicted in Figure 2 for the test at $P = 3$ N/mm, $\delta = 80$ µm for 100,000 cycles. The fretting log is averaged into a mean fretting loop, whose shape indicates that the test is run under gross slip conditions. The value of the tangential force also yields the macroscopic Coulomb's friction coefficient $\mu = 0.9$.

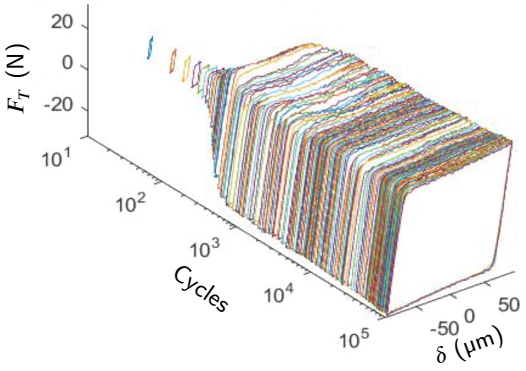

Figure 2: Fretting log for the wear test at $P = 30$ N, $\delta = 80$ µm for 100,000 cycles [26].

After the tests, a first observation of the wear scars is made with Scanning Electron Microscopy (SEM, Figure 3). The samples show bilateral wear on both the cylinder and the plane surfaces. A morphological description of the wear scars is given using laser interferometry (Figure 4). The 3D wear scars are averaged along the cylinder axis to get equivalent 2D wear profiles (Figure 5). For every test, the cylinder displays a U-shaped wear profile, while the plane shows a W to U shape transition at displacement amplitude around $\delta = 100$ µm: for displacement amplitudes lower than

$\delta = 100$ µm the plane has a W-shaped profile (Figure 5 at $\delta = 80$ µm), and for higher amplitudes it has a U shape.

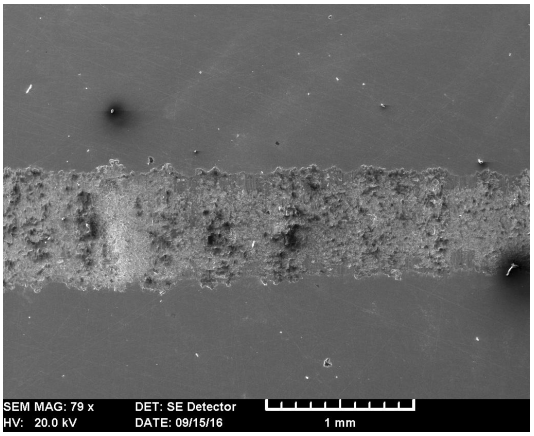

Figure 3: SEM view of the worn plane surface [26].

Complementary investigations with Energy-Dispersive X-ray spectroscopy (EDX) inform about the chemical composition of the scars. They show that in case of a W-shaped scar, the cluster at the center of the scar is composed of oxides, leading to the conclusion that this pile is made of wear debris, despite the gross slip conditions. Marc also mentions that the beads on the edges of the W-shaped wear profile of the plane result from plastic deformations.

2.2. Wear model

The wear law used in this work relates wear to frictional dissipated energy. Several studies established that a linear relationship between the worn volume V_w and the energy dissipated by friction E_d can be observed for both uni- or bidirectional motion [7, 8]. This leads to formulate the Equation (1) in which α is the wear coefficient of the energetic wear law:

$$V_w = \alpha E_d. \tag{1}$$

In case of a constant coefficient of friction μ, it is analogous to the widely used Archard's model. The wear equation used in the present study is a local version of the energetic wear law which was formulated by Fouvry et al. [30]. It is expressed in Equation (2) and relates the wear depth h at some point x of the surface to the dissipated energy density per unit area e_d at that point:

$$h(x) = \alpha e_d(x). \tag{2}$$

It should be noted that the use of Archard's law or, equivalently, energetic wear law, has recently been questioned especially by Zhu and Shipway [31]. They argue that as wear evolves, debris ejection can become more difficult due to the increase in the contact dimensions. Thus, debris ejection may become the wear rate-determining process instead of debris formation, and in that case the wear rate decreases. Accounting for that effect, they propose a modified relation between wear volume and dissipated energy for cylinder/plane contacts:

$$V_w = \alpha E_d^{0.75}. \tag{3}$$

In the present work however, wear evolution is considered to be following the classical energetic law given in Equation 1. Indeed, the experimental results obtained by Marc [26] for fretting wear tests for different normal forces, displacement amplitudes or numbers of cycles show a linear relationship between the worn volume and the cumulative dissipated energy. This leads to the assumption that in this case, debris are readily ejected out of the contact and that debris formation is the mechanism that governs wear rate. Based on their data, Marc et al. then determine the wear coefficient α for both the 316L cylinder and the 304L plane (Table 1).

Table 1
Wear coefficient values for the 316L SS cylinder and the 304L SS plane [26].

α_{cyl} (mm^3/mJ)	α_{pla} (mm^3/mJ)
2.3241×10^{-8}	3.1383×10^{-8}

3. Finite element model

A numerical framework is developed in order to predict wear kinetics under fretting conditions. Computations are performed using the finite element code CAST3M [32]. The results obtained are then compared with the experimental data presented previously.

In order to represent the case study of Marc, a two-dimensional plane strain finite element model is defined using 4-nodes bilinear elements. The model represents a cylinder in contact with a plane (Figure 6). In the vicinity of the contact zone, the element size is 6 µm. As in the experimental tests, the cylinder radius is $R = 4.85$ mm. The material behavior is considered as linear elastic, with the same Young's modulus and Poisson's ratio for both solids ($E = 200$ GPa and $\nu = 0.3$).

A zero-displacement condition is imposed on the bottom and side lines of the plane, and the equality of the vertical displacement of all the cylinder top line nodes is enforced (thus preventing rigid body rotations). Moreover, a uniformly distributed normal pressure is applied on top of the cylinder to account for the normal load $P = 3$ N/mm, and a cyclic triangular horizontal displacement is imposed on the cylinder with an amplitude $\delta = 80$ µm. Each fretting cycle is divided into 64 time steps.

Enforcing the contact conditions at the interface is not trivial and several methods exist. Here, frictional contact conditions are defined using the Lagrange multipliers method and a node-to-segment formulation [33]. The contact surface of the cylinder is defined as the impactor surface while the top surface of the plane is defined as the target surface.

Wear is computed at the end of each fretting cycle based on the accumulated dissipated energy over the cycle. A nodal displacement is imposed accordingly at the end of each cycle following a procedure described in Section 4.

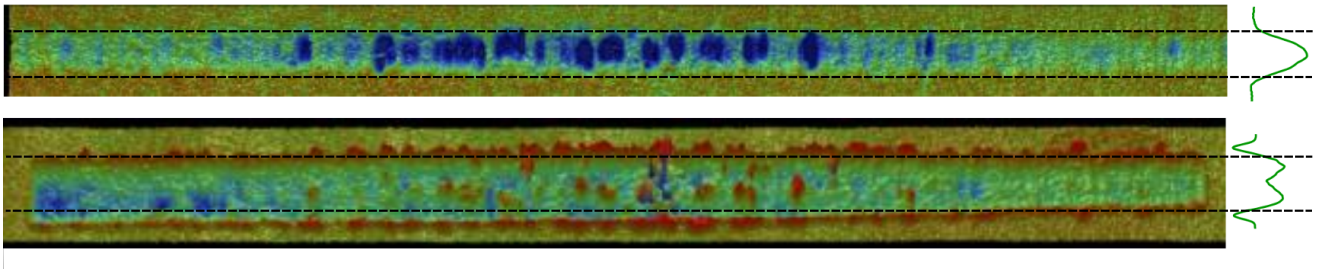

Figure 4: Wear scars on the cylinder (top) and the plane (bottom) obtained by interferometry for the wear test at $P = 30$ N, $\delta = 80$ µm for 100,000 cycles, and averaged 2D equivalent wear profiles [26].

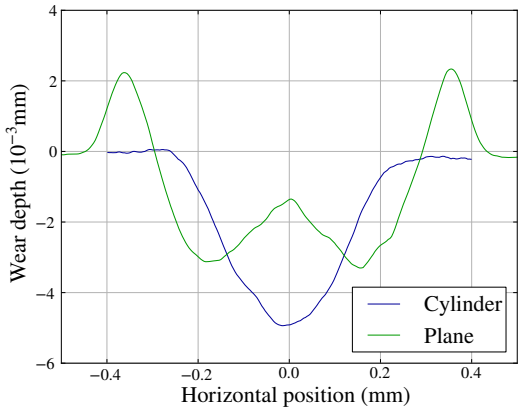

Figure 5: Equivalent wear profiles on the cylinder and the plane for the test at $P = 30$ N, $\delta = 80$ µm for 100,000 cycles [26].

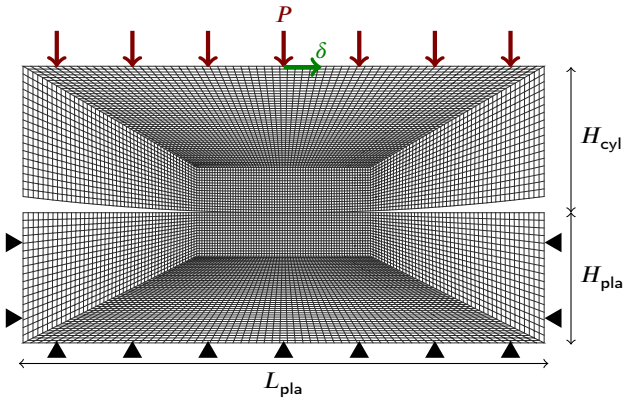

Figure 6: 2D finite element mesh of the cylinder/plane contact problem.

4. Simulation strategies

The objective of the simulation is to evaluate a function $h(x, n)$ representing the wear depth at each point x in $[-L/2, L/2]$ of the contacting surfaces for each fretting cycle n in $[0, N_{cyc}]$, L being the horizontal dimension of the model and N_{cyc} the total number of fretting cycles.

Here, the variable n is supposed to be a real number and plays the role of a pseudo time variable. In this representation, a fretting cycle is set to be an elementary pseudo time step. In other words, the problem can be described as a multi time scales problem, with the short time scale referring to what happens within a fretting cycle, whereas the long time scale is driven by the cycle number variable n [34]. This process is represented in Figure 7. First, the computation of the wear profile increment over a cycle is presented in Section 4.1, describing the short time scale. Then, Section 4.2 describes the cycle jump method used to manage the long time scale.

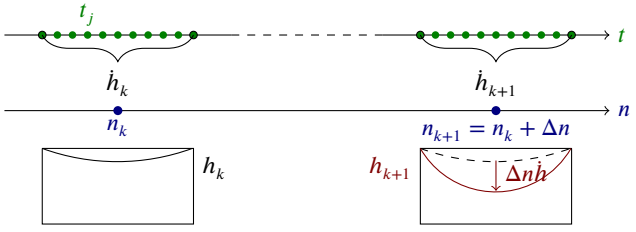

Figure 7: Representation of the double time scale process

4.1. Computation of the wear kinetics: short time scale description

The wear simulation routine consists in updating the surface geometries at the end of each fretting cycle to account for material loss. Wear is represented through a nodal displacement technique. The computed wear profile is applied to the mesh by moving the surface nodes, and the bulk nodes are consequently moved in order to prevent element distortion, as done for example by Kim et al. [16]. The third body is not represented.

At each time step of a cycle n, the non-linear frictional contact problem is solved yielding the nodal tangential reaction force per unit surface λ_t and the nodal sliding distance d. At each node x, the dissipated energy density over the time step j is then given by:

$$e_{d,j}(x, n) = \lambda_{t,j}(x, n) d_j(x, n) \tag{4}$$

and the sum over all the time steps of a fretting cycle yields the accumulated dissipated energy density over that fretting cycle:

$$e_{\mathrm{d}}(x,n) = \sum_j e_{\mathrm{d},j}(x,n). \tag{5}$$

The nodal wear depth increment over the cycle n is denoted $\dot{h}$ and is referred to as the wear kinetics, namely the amount of wear that is locally generated per fretting cycle. It is expressed in Equation (6) as the derivative of the wear depth h with respect to the fretting cycle n:

$$\dot{h}(x,n) = \frac{\partial h}{\partial n}(x,n). \tag{6}$$

According to the wear law (2) defined in Section 2.2, it is obtained by multiplying the dissipated energy density profile by the wear coefficient α:

$$\dot{h}(x,n) = \alpha e_{\mathrm{d}}(x,n) \tag{7}$$

In the following, the node x will be omitted in the expressions for the sake of notation simplicity.

4.2. Cycle jump: long time scale description

In order to reduce the computational cost, a cycle jump technique is used. For this purpose, an acceleration factor Δn is defined as the step between two consecutive computed fretting cycles:

$$\Delta n = n_{k+1} - n_k \tag{8}$$

with k in $\{1, 2, \dots, K\}$, leading to the effective computation of only K cycles. At first, the acceleration factor is set to be constant. Then, an adaptive cycle jump process is defined with a variable acceleration factor (see Section 4.4). In that case, the acceleration factor after cycle n_k is denoted Δn_k.

Consequently, the wear profile will be computed iteratively. An initial wear state h_0 is defined, typically as $h_0(x) = 0$ for all nodes x, and then for every computed cycle n_k:

$$h_{k+1} = h_k + \int_{n_k}^{n_{k+1}} \dot{h}(n) dn \tag{9}$$

with h_k a simplified notation for $h(x, n_k)$ and $\dot{h}$ the wear kinetics defined in Section 4.1 as the derivative of h with respect to n. Different integration schemes can be considered to compute the expression in Equation (9), which are discussed next.

4.3. Explicit and implicit cycle jump integration schemes

The simplest way to compute the integral term in Equation (9) is to approximate it using a forward Euler explicit integration scheme. It relates the wear profile h_{k+1} at cycle n_{k+1} to the wear kinetics calculated at the previous cycle n_k, as expressed in Equation (10):

$$h_{k+1} = h_k + \Delta n\, \dot{h}_k \tag{10}$$

The use of Runge-Kutta schemes is also explored. We limit ourselves here to the use of Runge-Kutta schemes of order 2 and 4. They are also explicit schemes as the wear profile h_{k+1} can be directly derived based on the knowledge of the wear profile h_k, but they require the computation of intermediate time steps. For instance, the relation between h_k and h_{k+1} according to the Runge-Kutta scheme of order 2 is expressed by:

$$h_{k+1} = h_k + \Delta n\, \dot{h}_{k+1/2} \tag{11}$$

where

$$\dot{h}_{k+1/2} = \dot{h}\left(h_k + \frac{1}{2}\Delta n\, \dot{h}_k\right). \tag{12}$$

These schemes are more time-consuming than the forward Euler scheme, as they require to compute respectively 2 or 4 times more fretting cycles. In return, we can expect them to be more reliable especially when a high acceleration factor is used.

Finally, a backward Euler implicit scheme is considered. It relates the wear profile at cycle n_{k+1} to the wear kinetics at that same cycle n_{k+1}, which depends itself on h_{k+1}:

$$h_{k+1} = h_k + \Delta n\, \dot{h}_{k+1}. \tag{13}$$

As the computation of $\dot{h}_{k+1}$ requires the knowledge of h_{k+1}, an iterative scheme is required to solve Equation (13). This is often made by the use of the Newton-Raphson algorithm, but this requires to compute the tangent term defined here by the derivative of the wear kinetics $\dot{h}$ with respect to the wear depth h. This computation is not straightforward and can be costly. Hence, a simpler fixed-point iteration scheme is used instead with a relaxation method in order to prevent non-convergence situations. It consists in progressively relaxing the increment between two consecutive iterations of the fixed-point scheme. As a result, the iterative algorithm for solving the backward Euler implicit scheme reads as follows:

- Initialization, $i = 0$:

$$h^0_{k+1} = h_k + \Delta n\, \dot{h}_k \tag{14}$$

- Iteration i: while the convergence is not achieved,

$$h^{i+1}_{k+1} = h^i_{k+1} + \frac{1}{2^{p_i}}\delta h^i_{k+1} \tag{15}$$

  where p_i is the relaxation exponent at iteration i and the increment δh^i_{k+1} is expressed:

$$\delta h^i_{k+1} = h_k + \Delta n\, \dot{h}^i_{k+1} - h^i_{k+1} \tag{16}$$

- Convergence when:

$$\frac{\|\delta h^i_{k+1}\|}{\|\Delta n\, \dot{h}_k\|} < 10^{-3}. \tag{17}$$

The relaxation exponent p_i is set to 0 for the first iteration, to 1 for the next two iterations, to 2 for the next four iterations, ..., to k for the next 2^k iterations, etc. It is noteworthy that if the relaxation exponent is equal to 0, then the classical expression for the fixed-point iteration is retrieved.

Note that this way of solving the implicit scheme may not be optimal, as the fixed-point iteration scheme does not ensure a quadratic convergence, which is the case for Newton-Raphson. In order to improve the convergence rate, other algorithms than the simple fixed-point scheme should be investigated.

4.4. Adaptive cycle jump

Finally, an adaptive cycle jump process is considered. In this case, the acceleration factor Δn_k is supposed to be variable and is computed at the end of each fretting cycle n_k. The reason for investigating an adaptive cycle jump technique lies in the observation that the computed wear kinetics profile changes quickly with cycles at the start of the computation, and then its shape changes progressively more slowly. Thus, it could be beneficial to gradually increase the acceleration factor throughout the computation.

Several studies proposed to use the maximal wear depth to control the acceleration factor [15, 25]. In that case, a maximal wear depth increment $\Delta h_{0,\max}$ is allowed between two consecutive computed cycles, and the acceleration factor Δn_k at cycle n_k is derived based on the computed maximum wear depth kinetics $\dot{h}_{\max}$:

$$\Delta n_k = \frac{\Delta h_{0,\max}}{\partial h_{\max}/\partial n} = \frac{\Delta h_{0,\max}}{\dot{h}_{\max}(n_k)}. \tag{18}$$

In the present paper, the strategy used to compute the acceleration factor is based on an estimate of the wear profile enlargement rate instead, which is an alternative never explored to the authors' knowledge. The enlargement rate is taken to be an indicator of the speed at which the shape of the computed profile changes. The faster the wear profile widens, the lower the acceleration factor. The width of the worn area is denoted l, and the enlargement rate $\dot{l}$ is its derivative with respect to the cycles n. The acceleration factor is expressed as follows:

$$\Delta n_k = \frac{\Delta l_0}{\partial l/\partial n} = \frac{\Delta l_0}{\dot{l}(n_k)} \tag{19}$$

where Δl_0 is the width increment expected between two consecutive computed cycles. The strategy used to estimate the enlargement rate $\dot{l}$ is discussed later in Section 5.1.

5. Results and discussion

5.1. Explicit wear simulation

The numerical process described is applied first with a forward Euler explicit integration scheme and a constant acceleration factor. In order to compare the numerical results with the experimental data, the computation is run on a total number of 100,000 cycles.

Preliminary computations on a low number of cycles show that unexpected oscillations may appear on the wear profiles, depending on the value of the acceleration factor (Figure 8). They arise from small perturbations in the computed contact reaction forces which are eventually reverberated on the dissipated energy distribution and the wear profile. These perturbations are amplified by the use of an acceleration factor, and the modification of the surface nodes position following a perturbed wear profile leads to instabilities.

These instabilities have been related by several authors [15, 17, 35]. Basseville et al. proposed to use a Gaussian smoothing function in order to eliminate the perturbations [36]. They used an exponential moving average to smooth the dissipated energy profile, which showed good results in removing the instabilities, but has the disadvantage of slightly altering the shape of the profile. Moreover, it requires to wisely choose the parameter of the smoothing function: a moving average with a too large bandwidth will alter the profile shape, while a too narrow one will not remove the instabilities. Here, the choice is made to not use smoothing techniques.

The results obtained in the present study show that there exists a critical acceleration factor value under which no oscillation is observed, and above which sharp oscillations quickly appear on the pressure profile. This critical value depends on the mesh density, and a finer mesh is detrimental regarding the instabilities. A linear relation is observed between the critical acceleration factor and the mesh size, which is depicted in Figure 9. A computation with an acceleration factor Δn is said to be unstable when the root mean square (RMS) error of the pressure profile of the 300$^{\text{th}}$ cycle compared to the same computation with $\Delta n = 1$ exceeds 5%. Studies show that in case of instabilities, they appear as early as the first fretting cycles, which we observe as well [15, 17]. This leads to the assumption that if no instability appears during the first 300 cycles, it will not appear later.

The same investigations are conducted with the Runge-Kutta schemes of order 2 and 4. Results show that even though they are more stable than the forward Euler scheme, they are not worth the computational cost increase. Indeed, these schemes require respectively 2 or 4 times more computations, and do not ensure a critical acceleration factor respectively 2 or 4 times greater than with the forward Euler scheme (Figure 9).

Consequently, a full computation was run on 100,000 cycles with an acceleration factor $\Delta n = 3$ and a forward Euler explicit scheme, thus ensuring a stable computation of wear profiles.

The wear kinetics profiles confirm that no instability occurs during the computation (Figure 10). Results show that the same amount of energy is dissipated at each fretting cycle, and thus the wear volume per cycle is constant. It implies that the wear kinetics profiles in Figures 10a and 10b respectively have a same integral, and only the spatial distribution changes. During the early cycles, the wear kinetics (or, equivalently, the dissipated energy) distribution

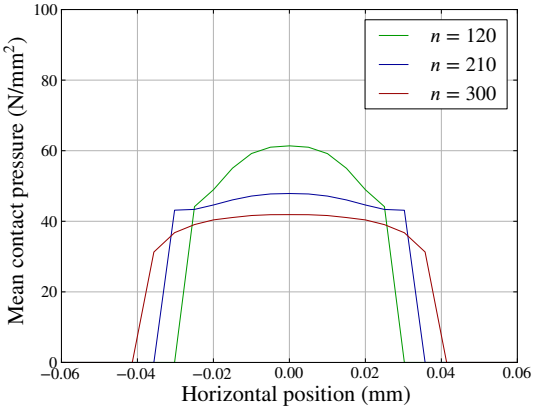

(a) Mesh size 5 µm, acceleration factor $\Delta n = 3$

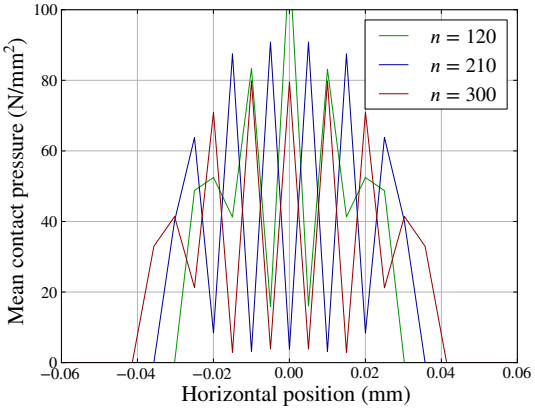

(b) Mesh size 5 µm, acceleration factor $\Delta n = 10$

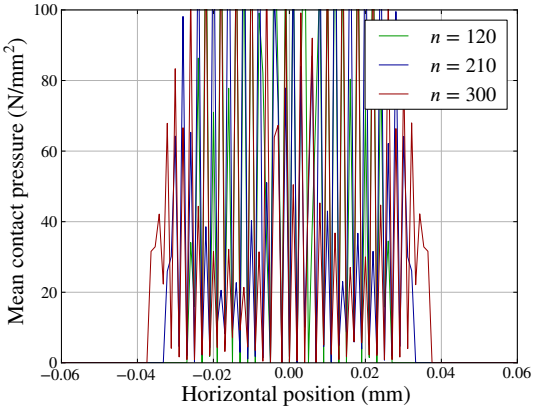

(c) Mesh size 1 µm, acceleration factor $\Delta n = 3$

Figure 8: Mean contact pressure profiles on the cylinder surface over a fretting cycle for computations with a forward Euler scheme (a) stable and (b),(c) unstable.

is localized at the center of the surfaces, and then spreads slightly.

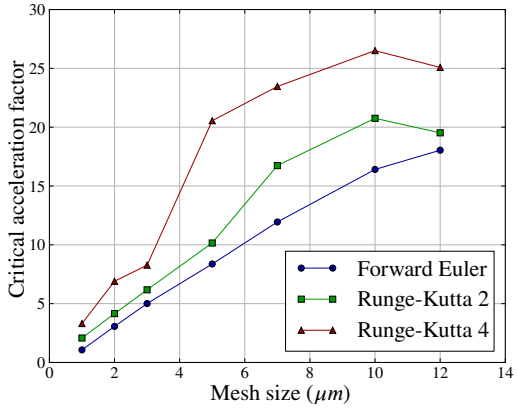

Figure 9: Limit of stability in terms of acceleration factor versus mesh size, for the forward Euler and Runge-Kutta of order 2 and 4 schemes.

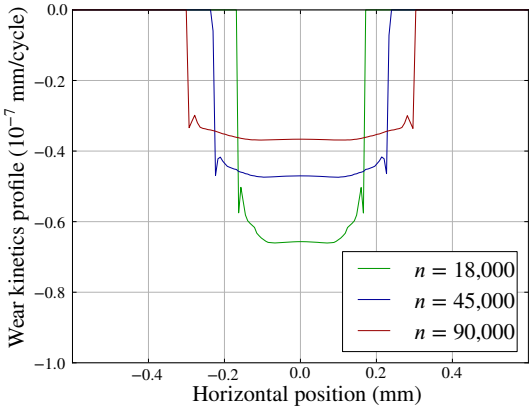

(a) Cylinder

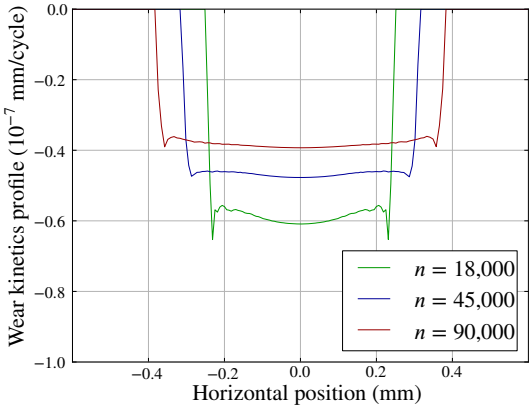

(b) Plane

Figure 10: Wear kinetics profiles on the (a) cylinder and (b) plane surfaces at cycles 18,000 ; 45,000 and 90,000 computed with a forward Euler integration scheme.

The evolution of the wear profiles on the cylinder and the plane surface are depicted in Figure 11. They show that the wear profiles are first located at the center of the surfaces, and then expand both in depth and width over the cycles.

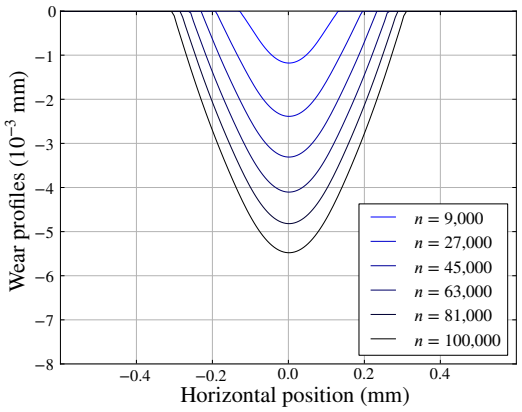

(a) Cylinder

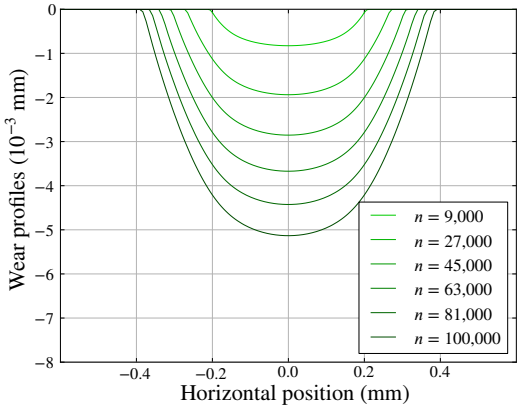

(b) Plane

Figure 11: Evolution of the wear profiles on the (a) cylinder and (b) plane surfaces over the cycles computed with a forward Euler integration scheme for $\Delta n = 3$.

In order to characterize the wear profiles evolution, the expansion of the width of the worn area is considered. Figure 12 shows that the width of the worn zone on both the cylinder and the plane expands very quickly during the early cycles, before the rate of evolution decreases. The discontinuities originate from the spatial discretization of the surfaces. Based on these numerical results, the width l of the worn area can be approximated with good accuracy by a power law of the form:

$$l(n) = l_0 + \kappa_1 n^{\kappa_2} \tag{20}$$

where l_0, κ_1 and κ_2 are the parameters of the approximation law and n the cycle. The approximated evolutions are shown in Figure 12 as well for comparison with the numerical results. In their paper of 2019, Zhu et al. [9] derive a geometrical relation between the wear volume and the wear scar width for cylinder/plane contacts, under the assumption that the displacement amplitude is negligible with respect to the width of the wear profile, such that both solids have the same wear scar width:

$$\frac{V_\mathrm{w}}{L} = R^2 \arcsin\left(\frac{l}{2R}\right) - \frac{l}{2}\sqrt{R^2 - \frac{l^2}{4}} \tag{21}$$

where V_w is the wear volume, L is the out-of-plane dimension of the contact and R is the cylinder radius. The relation they obtained is compared with the numerical results from the present work, using the relation between the wear volume and the cycle number. Figure 12 shows similar tendencies between the relation from Zhu et al. and the evolutions obtained numerically. The discrepancy is related to the fact that the hypothesis made by Zhu et al. is not fulfilled here, namely both solids do not have the same width for the worn area.

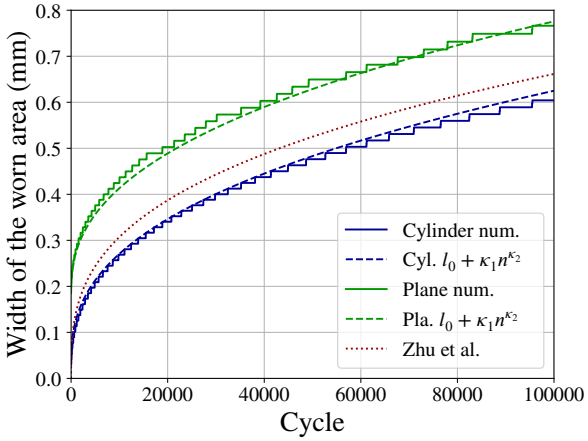

Figure 12: Evolution of the wear profiles widths along the 100,000 computed cycles. Comparison with the approximated evolution with a power law, and with the relation derived by Zhu et al. [9].

Eventually, the final wear profiles after 100,000 cycles are compared with those obtained experimentally (Figure 13). On the cylinder surface, the computed wear profile has the same U shape as in the experiment, though slightly deeper and wider. On the plane surface however, the W-shaped profile obtained experimentally could not be represented by the model. This was expected, given that the proposed model does not account for neither the third body effects nor plasticity.

5.2. Implicit wear simulation with constant acceleration factor

Afterwards, computations are performed using the backward Euler implicit integration scheme presented earlier in Section 4.3. Preliminary tests show that, unlike with the forward Euler scheme, no instability has been observed as far as it has been tried. For example, as depicted in Figure 14, a computation with a mesh size of 5 µm and an acceleration factor $\Delta n = 30$ is highly unstable with the forward Euler

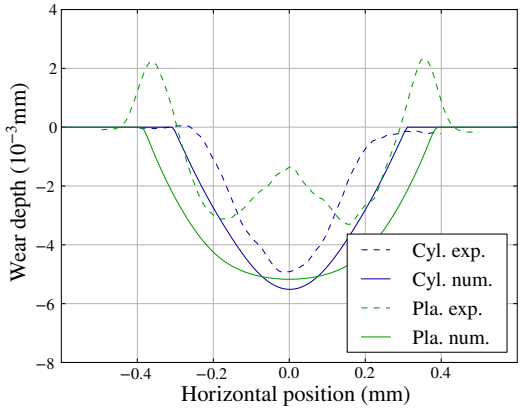

Figure 13: Comparison of the computed wear profiles with the experimental data on the cylinder and the plane surfaces after 100,000 fretting cycles.

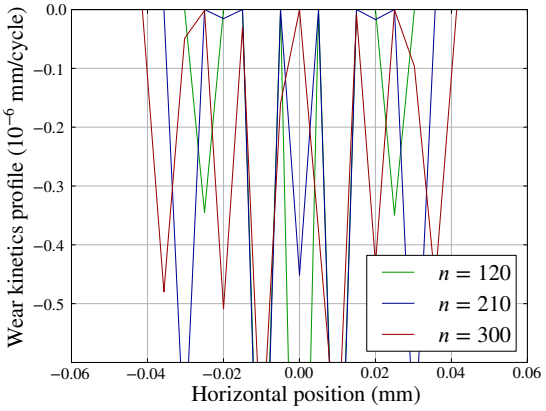

(a) Forward Euler explicit scheme

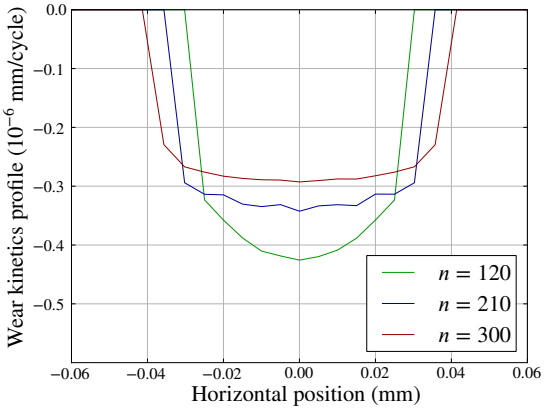

(b) Backward Euler implicit scheme

Figure 14: Wear kinetics profiles obtained on the cylinder surface with (a) a forward Euler explicit integration scheme and (b) a backward Euler implicit integration scheme on a computation with mesh size 5 µm and acceleration factor $\Delta n = 30$.

scheme, but stable with the backward Euler scheme. The use of a backward Euler scheme thus allows to take an acceleration factor beyond the stability limit of the forward Euler scheme. However, a certain number of iterations are required for the scheme to converge, which increases the computational costs. The issue is then to determine whether the convergence is fast enough to compete with the forward Euler scheme.

A computation is run on 100,000 fretting cycles with a constant acceleration factor $\Delta n = 30$. The evolution of the number of iterations required for the convergence of the backward Euler cycle jump integration scheme is shown in Figure 15. First, it can be seen that a few cycles do not reach convergence after a maximum number of iterations of 25. As they represent less than 10 computed cycles out of several thousands, we propose to leave these non-convergences aside. Apart from these few cycles, the number of iterations per cycle jump is between 5 and 10 for the early cycles, and decreases quickly: after a few hundred cycles, the implicit scheme converges often in one or two iterations. However, as it can be seen in Figure 15, some cycles converge more slowly (4 or 5 iterations). These slowly converging cycles are regularly spaced and perfectly match the cycles at which the wear profiles enlarge. In other words, the cycles at which the implicit scheme converges slowly are the same as the cycles at which the evolution of the wear profile width (Figure 12) has a discontinuity. According to the observations made on Figure 12, these discontinuities happen frequently in the early cycles, and then occur less and less often. These remarks support the idea of using an adaptive acceleration factor based on the wear profile enlargement rate: the faster the wear profile enlarges, the lower the acceleration factor, and vice-versa.

In the end, the wear profile after 100,000 fretting cycles is obtained by computing only 7,353 cycles overall, taking the iterations into account (Figure 17). This yields an equivalent acceleration factor $\Delta n_{\text{eq}} = 13.6$ where Δn_{eq} is defined by the ratio between the total number of cycles and the number of effectively computed cycles.

In addition, the final wear profiles obtained are the same as with the explicit scheme: the RMS error between the results of the different procedures is lower than 0.01%.

5.3. Implicit wear simulation with adaptive acceleration factor

Eventually, the computation is run with a variable acceleration factor. As discussed in Sections 4.4 and 5.1, the adaptive cycle jump technique is controlled by an estimate of the wear profile enlargement rate $\dot{l}$. The approximation of the wear profile width l expressed in Equation (20) yields:

$$\dot{l}(n) = \kappa_1 \kappa_2 n^{\kappa_2 - 1}. \tag{22}$$

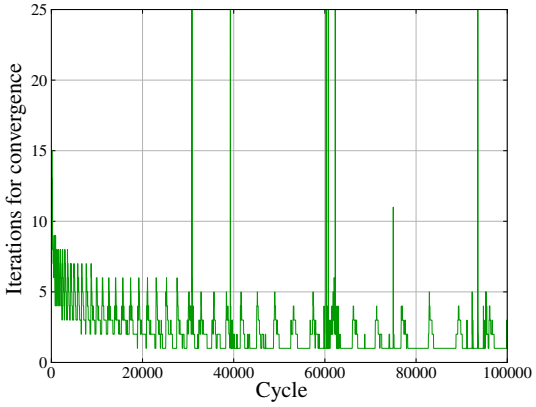

Figure 15: Number of iterations required for the convergence of the wear profile for each computed cycle with a backward Euler scheme and $\Delta n = 30$.

Following Equation (19) the variable acceleration factor is then given by:

$$\Delta n_k = \frac{\Delta l_0}{\kappa_1 \kappa_2} n_k^{1-\kappa_2}. \tag{23}$$

The parameters κ_1 and κ_2 are estimated and reevaluated on a regular basis throughout the computation using a Levenberg-Marquardt algorithm. This algorithm aims at solving non-linear least square problems and is used here to find the best fit κ_1 and κ_2 parameters with respect to the computed wear profile enlargement rate.

Because this technique would give very low values for the acceleration factor during the first cycles, a lower bound $\Delta n_{\min}$ is defined. Therefore, the value used for the acceleration factor is derived as follows:

$$\Delta n_k = \max\left(\frac{\Delta l_0}{\kappa_1 \kappa_2} n_k^{1-\kappa_2}, \Delta n_{\min}\right). \tag{24}$$

The computation is run with $\Delta n_{\min} = 30$.

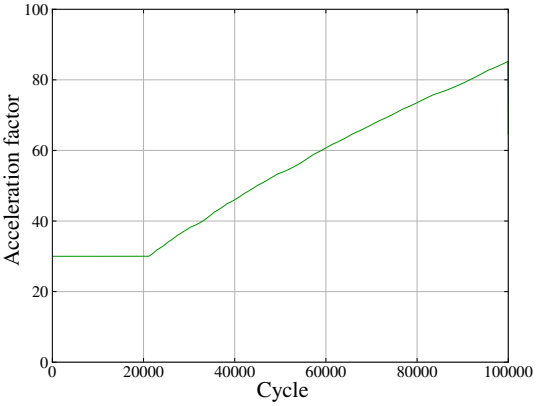

Figure 16: Evolution of the adaptive acceleration factor

Figure 16 shows the evolution of the acceleration factor through the computation. It increases progressively to reach a value over 80 at the end. This computation required 6,704 cycles overall, thus yielding an equivalent acceleration factor of $\Delta n_{\text{eq}} = 14.9$. Figure 17 shows the evolution of the number of cycles required to compute the wear profile after a given number of fretting cycles. It illustrates the efficiency of the implicit scheme to compute a high number of cycles. The greater the number of computed cycles, the lower the computational cost per cycle with these procedures. Moreover, using an adaptive cycle jump is beneficial for high cycle computations.

Table 2
Total number of computed cycles

Explicit, $\Delta n = 3$	Implicit, $\Delta n = 30$	Implicit, adaptive Δn
33,334	7,353	6,704

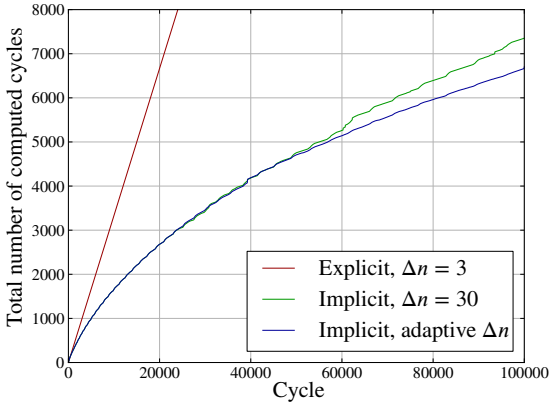

Figure 17: Evolution of the number of effectively computed cycles through the computation of 100,000 fretting cycles

Table 2 compares the number of cycle computations required to get the wear profiles after 100,000 cycles for the forward Euler explicit scheme at $\Delta n = 3$, the backward Euler implicit scheme at $\Delta n = 30$, and with a variable acceleration factor. For the implicit scheme, the number of computed cycles includes the number of iterations to convergence.

6. Conclusion

The simulation framework presented here enables to compute wear occurring at the contact between two solids under fretting solicitations. The interest of this kind of simulation lies in the fact that it can derive local quantities (wear depth distribution, contact stresses, distribution of the dissipated energy density, etc.) based on global observations from experimental tests: total wear volume, total dissipated energy.

For the sake of computational cost, a cycle jump technique is used and different integration schemes are investigated. The use of an explicit scheme can lead to unexpected oscillations which limits the acceleration factor value. On the opposite, results show that an implicit scheme succeeds to prevent these instabilities, and its convergence is fast enough

to decrease the computational cost. As a consequence, the use of an implicit cycle jump integration scheme is recommended. In addition, choosing an adaptive acceleration factor based on the wear profile enlargement rate is beneficial for high cycles.

The wear profiles obtained numerically and experimentally are similar to some extent. In the absence of plastic deformation and third body trapped in the interface, the comparison of the wear profiles obtained numerically with the experimental data shows a good accuracy. Both profiles have a U shape with similar width and depth. However, some experimental profiles show a W shape that our simulation process has more trouble representing. As a result, the simulation framework developed is especially suitable when debris transport out of the contact is easily achieved.

In order to better capture the complex processes involved in wear damage, including the effects of third body and plastic behavior would be a valuable asset. Regarding plasticity, taking it into account is not straightforward when using a cycle jump. As a matter of fact, the knowledge of the plastic strains evolution during one cycle gives little to no information on how it will evolve through the next cycles. Different regimes exist: elastic or plastic shakedown, or ratcheting, and extrapolating the behavior of a single cycle seems expeditious.

Acknowledgments

This work has been achieved within the framework of the French Nuclear Institute (Institut Tripartite CEA-EDF-Framatome).

References

[1] O. Vingsbo, S. Söderberg, On fretting maps, Wear 126 (1988) 131–147.

[2] L. Vincent, Y. Berthier, M. C. Dubourg, M. Godet, Mechanics and materials in fretting, Wear 153 (1992) 135–148.

[3] P. L. Ko, G. Knowles, M. C. Taponat, Friction characteristics and the wear process of metal pairs in sliding contacts - with applications to modelling wear of power plant components, Wear 213 (1997) 148–158.

[4] G. Kermouche, A.-L. Kaiser, P. Gilles, J. M. Bergheau, Combined numerical and experimental approach of the impact-sliding wear of a stainless steel in a nuclear reactor, Wear 263 (2007) 1551–1555.

[5] H. C. Meng, K. C. Ludema, Wear models and predictive equations - their form and content, Wear 181 (1995) 443–457.

[6] J. F. Archard, Contact and rubbing of flat surfaces, Journal of Applied Physics 24 (1953) 981–988.

[7] S. Fouvry, P. Kapsa, L. Vincent, Quantification of fretting damage, Wear 200 (1996) 186–205.

[8] M. Z. Huq, J.-P. Celis, Expressing wear rate in sliding contacts based on dissipated energy, Wear 252 (2002) 375–383.

[9] T. Zhu, P. Shipway, W. Sun, The dependence of wear rate on wear scar size in fretting; the role of debris (third body) expulsion from the contact, Wear 440-441 (2019).

[10] S. Baydoun, P. Arnaud, S. Fouvry, Modelling adhesive wear extension in fretting interfaces: An advection-dispersion-reaction contact oxygenation approach, Tribology International 151 (2020) 106490.

[11] P. Shipway, A. Kirk, C. Bennett, T. Zhu, Understanding and modelling wear rates and mechanisms in fretting via the concept of rate-determining processes - Contact oxygenation, debris formation and debris ejection, Wear 486-487 (2021).

[12] L. Johansson, Numerical simulation of contact pressure evolution in fretting, Journal of Tribology 116 (1994) 247–254.

[13] P. Põdra, S. Andersson, Simulating sliding wear with finite element method, Tribology International 32 (1999) 71–81.

[14] M. Oqvist, Numerical simulations of mild wear using updated geometry with different step size approaches, Wear 249 (2001) 6–11.

[15] I. R. McColl, J. Ding, S. B. Leen, Finite element simulation and experimental validation of fretting wear, Wear 256 (2004) 1114–1127.

[16] N. H. Kim, D. K. Won, D. Burris, B. Holtkamp, G. R. Gessel, P. Swanson, W. G. Sawyer, Finite element analysis and experiments of metal/metal wear in oscillatory contacts, Wear 258 (2005) 1787–1793.

[17] C. Mary, S. Fouvry, Numerical prediction of fretting contact durability using energy wear approach: Optimisation of finite-element model, Wear 263 (2007) 444–450.

[18] C. Paulin, S. Fouvry, C. Meunier, Finite element modelling of fretting wear surface evolution: Application to a Ti-6al-4v contact, Wear 264 (2008) 26–36.

[19] A. L. Mohd Tobi, J. Ding, G. Bandak, S. B. Leen, P. H. Shipway, A study on the interaction between fretting wear and cyclic plasticity for Ti-6al-4v, Wear 267 (2009) 270–282.

[20] S. Basseville, H. Proudhon, E. Héripré, G. Cailletaud, Étude numérique des paramètres affectant les profils d'usure en fretting, Matériaux & Techniques 101 (2013) 207.

[21] H. Yang, I. Green, Fretting wear modeling of cylindrical line contact in plane-strain borne by the finite element method, Journal of Applied Mechanics, Transactions ASME 86 (2019).

[22] P. Arnaud, S. Fouvry, A dynamical FEA fretting wear modeling taking into account the evolution of debris layer, Wear 412-413 (2018) 92–108.

[23] H. Proudhon, J. Savkova, S. Basseville, V. Guipont, M. Jeandin, G. Cailletaud, Experimental and numerical wear studies of porous Reactive Plasma Sprayed Ti–6al–4v/TiN composite coating, Wear 311 (2014) 159–166.

[24] P. Arnaud, S. Baydoun, S. Fouvry, Modeling adhesive and abrasive wear phenomena in fretting interfaces: A multiphysics approach coupling friction energy, third body and contact oxygenation concepts, Tribology International 161 (2021).

[25] S. Garcin, S. Fouvry, S. Heredia, A FEM fretting map modeling: Effect of surface wear on crack nucleation, Wear 330 (2015) 145–159.

[26] E. Marc, Analyse de la réponse tribologique d'un contact cylindre/plan soumis à des sollicitations de fretting sous chargement complexe : influence d'une solution Lithium-Bore, Thèse de doctorat, Université de Lyon, 2018.

[27] P. J. Loew, L. H. Poh, B. Peters, L. A. A. Beex, Accelerating fatigue simulations of a phase-field damage model for rubber, Computer Methods in Applied Mechanics and Engineering 370 (2020).

[28] E. Marc, S. Fouvry, C. Phalippou, H. Maitournam, Fretting wear response of a nitrided 316l SS/304l SS interface: Effect of lithium/bore liquid environment, Surface and Coatings Technology 308 (2016) 226–235.

[29] E. Marc, S. Fouvry, O. Graton, C. Phalippou, H. Maitournam, Fretting wear of a nitrided 316l/304l contact subject to in-phase normal force fluctuation in dry and lithium-boron solution: An R-P-friction energy wear approach, Wear 376 (2017) 690–704.

[30] S. Fouvry, T. Liskiewicz, P. Kapsa, S. Hannel, E. Sauger, An energy description of wear mechanisms and its applications to oscillating sliding contacts, Wear 255 (2003) 287–298.

[31] T. Zhu, P. Shipway, Contact size and debris ejection in fretting: The inappropriate use of Archard-type analysis of wear data and the development of alternative wear equations for commonly employed non-conforming specimen pair geometries, Wear 474-475 (2021).

[32] Cast3m, 2021. URL: http://www-cast3m.cea.fr/.

[33] P. Wriggers, Computational Contact Mechanics, 2 ed., Springer-Verlag Berlin Heidelberg, 2006.

[34] J. Lengiewicz, S. Stupkiewicz, Continuum framework for finite element modelling of finite wear, Computer Methods in Applied

Mechanics and Engineering 205-208 (2012) 178–188.

[35] S. Mukras, N. H. Kim, W. G. Sawyer, D. B. Jackson, L. W. Bergquist, Numerical integration schemes and parallel computation for wear prediction using finite element method, Wear 266 (2009) 822–831.

[36] S. Basseville, M. Niass, D. Missoum-Benziane, J. Leroux, G. Cailletaud, Effect of fretting wear on crack initiation for cylinder-plate and punch-plane tests, Wear 420 (2019) 133–148.